# Directed Growth of Virus Nanofilaments on a Superhydrophobic Surface

Giovanni Marinaro,[†,‡] Manfred Burghammer,[†,#] Luca Costa,[†] Thomas Dane,[†] Francesco De Angelis,[‡] Enzo Di Fabrizio,[§,⊥] and Christian Riekel*[,†]

[†]ESRF-European Synchrotron Radiation Facility, CS 40220, F-38043 Grenoble Cedex 9, France
[‡]Nanostructures Department, Istituto Italiano di Tecnologia, Via Morego 30, Genova 16163, Italy
[§]Physical Science and Engineering Divisions, KAUST (King Abdullah University of Science and Technology) , Jeddah, Saudi Arabia
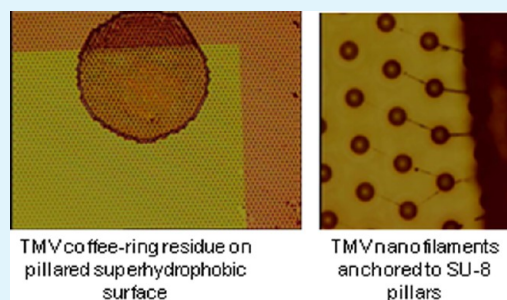[⊥]BIONEM Lab, University of Magna Graecia, Campus Salvatore Venuta, Viale Europa, 88100 Germaneto-Catanzaro, Italy
[#]Department of Analytical Chemistry, Ghent University, Krijgslaan 281, S12B-9000 Ghent, Belgium

Ⓢ *Supporting Information*

**ABSTRACT:** The evaporation of single droplets of colloidal tobacco mosaic virus (TMV) nanoparticles on a superhydrophobic surface with a hexagonal pillar-pattern results in the formation of coffee-ring type residues. We imaged surface features by optical, scanning electron, and atomic force microscopies. Bulk features were probed by raster-scan X-ray nanodiffraction. At ∼100 pg/µL nanoparticle concentration, the rim of the residue connects to neighboring pillars via fibrous extensions containing flow-aligned crystalline domains. At ∼1 pg/µL nanoparticle concentration, nanofilaments of ≥80 nm diameter and ∼20 µm length are formed, extending normal to the residue-rim across a range of pillars. X-ray scattering is dominated by the nanofilament form-factor but some evidence



TMV coffee-ring residue on pillared superhydrophobic surface

TMV nanofilaments anchored to SU-8 pillars

for crystallinity has been obtained. The observation of sheets composed of stacks of self-assembled nanoparticles deposited on pillars suggests that the nanofilaments are drawn from a structured droplet interface.

**KEYWORDS:** *droplet microfluidics, superhydrophobic surface, virus nanoparticles, nanofilaments, X-ray nanodiffraction*

## INTRODUCTION

Nucleation and crystallization processes during polymer extrusion can be probed for laboratory-scale extruders by synchrotron radiation (SR) small-angle (SAXS) and wide-angle (WAXS) X-ray scattering (summarized here as X-ray diffraction; XRD).[1] Local deformation and fracture zones in fibers and other extruded parts can be spatially resolved by raster-scan microbeam XRD (µXRD).[2] Biopolymers are, however, often only available in small quantities, requiring scaled-down devices for microstructural studies of assembly processes. Indeed, fibroin protein self-assembly can be probed using continuous-flow microfluidics combined with XRD.[3,4]

The aim of this article is exploring a further reduction of sample volumes by making use of digital microfluidics[5] and probing bulk assemblies by nanobeam XRD (nanoXRD) as well as surface features by optical microscopy (OM), atomic force microscopy (AFM) and scanning electron microscopy (SEM). Indeed, ultrasmall quantities of colloidal biological particles can be concentrated during evaporation of discrete droplets on a superhydrophobic surface (SHS) under quasi contact-free conditions.[6] The evaporation results in convective-flow mediated mass transport and the formation of a viscous interface-layer which is at the origin of self-assembly processes.[6] Similar processes occur on wetting surfaces resulting in coffee-ring type residues.[7] Shear- and capillary-flow alignment at the

droplet interface on a SHS allows generating filamentary morphologies. Indeed, λ-DNA nanofilaments, composed of an assembly of few molecular chains, can be obtained from ultradilute droplets on pillared Si-SHSs.[8] This process does not, however, involve large-scale self-assembly as the length of the molecular chains scales with the pillar distance.[9]

We will explore in this text self-assembly of tobacco mosaic virus (TMV) nanoparticles[10] on a pillared SHS extending experiments on TMV self-assembly on a wetting surface.[11] The rodlike particles have a length of ∼300 nm, a diameter of ∼18 nm with a ∼4 nm central bore.[12,13] TMV shows a rich phase diagram forming notably several liquid crystalline phases depending on the salt concentration and ionic strength (For a review see:[14]). The nanoparticles show head-to-tail self-assembly properties[15] and provide access to supramolecular materials such as 2D- and 3D-aggregates.[11,16−19] The potential for forming filamentous morphologies by self-assembly is suggested by the observation of highly oriented domains down
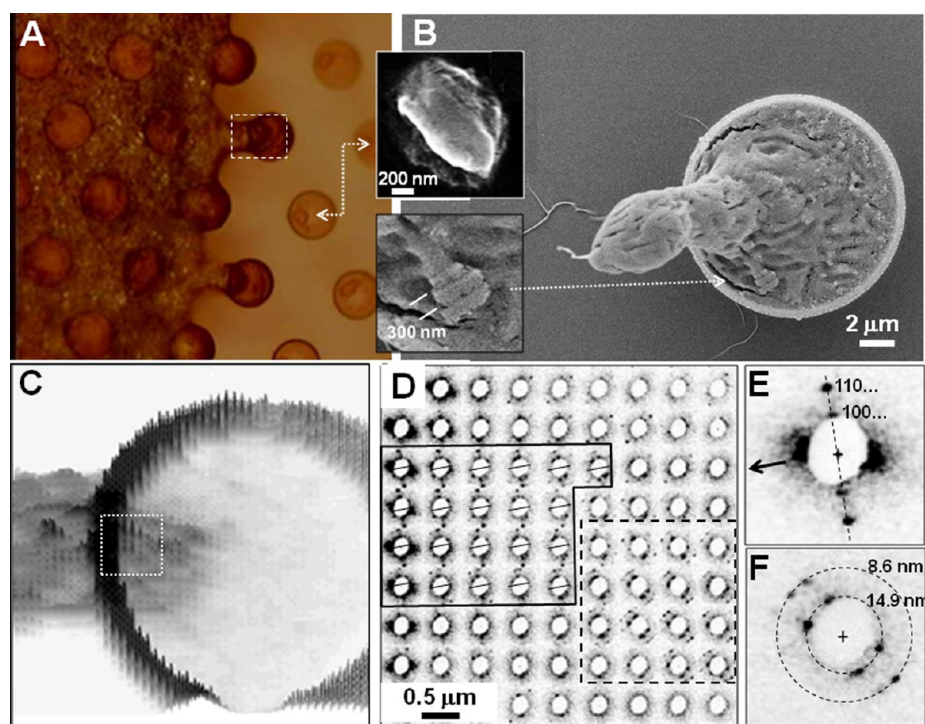
**Figure 1.** (A) OM-image of residue. A residue patch on a pillar is indicated by an arrow. The inset shows a SEM image of a patch. (B) SEM image of pillar with residue-extension, separated from rim. The inset shows a zoom of a patch with stacked rows of nanoparticles. (C) Pseudo 3D display of 32 × 32 binned RD-image of dashed area in A. The angular range of the pixels is limited to $Q_{max} \approx 0.4$ nm$^{-1}$ ($Q = 4\pi\sin\theta\lambda^{-1}$; with $\lambda$, wavelength; $\theta$, Bragg angle). The intense ring is due to edge scattering from the SU-8 pillar.[33] (D) 1 × 1 binned RD-image of dashed area in C. The solid line delineates a domain with homogeneous orientation of $hk0$ reflections. The lines in each pattern indicate the direction of the TMV fiber axis (projection). The dashed line corresponds to an area with multiple overlapping patterns. (E) NanoXRD pattern from domain with equatorial scattering. The arrow corresponds to the fiber axis direction. (F) NanoXRD pattern from dashed line area revealing overlapping domains. The rings correspond to the 100/110 (and symmetry-equivalent) reflections of the primitive hexagonal TMV lattice with $a = b \approx 17$ nm.[11]

to the micrometer-scale at the rim of a coffee-ring type residue.[11] Exploring the range of TMV morphologies formed at surfaces is also of practical interest for bottom-up assembly of functional micro/nano biological systems.[20−24] Indeed, the central bore of a TMV nanoparticle can be filled by metal nanoparticles resulting in electrically conductive nanowires.[25,26] Composite TMV nanofilaments or bundles can be assembled after coating the nanoparticles by a metallic conducting layer followed by surface polymerization.[27−29] Metal-coated TMV nanoparticles are envisaged as 3D hierarchical electrodes in high-performance microbatteries.[30]

## ■ EXPERIMENTAL SECTION

**Substrates.** We used SHSs with a regular hexagonal pillar pattern of 30 $\mu$m pitch. Droplets were deposited for laboratory experiments on a Si-SHS with 10 $\mu$m diameter and 10 $\mu$m high pillars on a ~500 $\mu$m thick Si-substrate.[6,31,32] NanoXRD experiments were performed using high X-ray transmission SHSs based on a thin Si$_3$N$_4$ membrane and SU-8 pillars.[33] Both regular and gradient pillar patterns were used. The surface of both types of SHSs was covered by a ~30 nm thick PTFE layer.

**Sample Deposition.** A ~12 ng/$\mu$L TMV colloidal nanoparticle solution containing potassium phosphate buffer salt[34] was diluted with deionized water by factor $1 \times 10^2$ and $1 \times 10^4$. Four to five microliter droplets were deposited on the SHSs by a pipet and left drying in air at room temperature.

**Imaging and Diffraction Techniques.** OM was performed with an inverted Olympus microscope using reflected light illumination. AFM imaging was performed with an Asylum Research CYPHER scanning probe microscope in tapping mode at the ESRF Surface Science Laboratory (see the Supporting Information). SEM images

were recorded with a ZEISS LEO 1530 SEM at 5 and 10 kV at the ESRF Microimaging Laboratory. A ~10 nm Au-layer was deposited by sputtering to avoid charging. NanoXRD experiments were performed at the ESRF ID13-beamline using a $\lambda = 0.08321$ nm monochromatic X-ray beam which was focused to a ~170 nm circular spot by refractive X-ray optics at the sample position.[33,35] NanoXRD experiments were performed in transmission geometry with the beam normal to the substrate. The sample was raster-scanned through the beam and a pattern was recorded at every step by a CCD camera with X-ray converter screen. Results are displayed as raster-scan diffraction images (RD-image) with "pixels" corresponding to individual patterns[36] (see the Supporting Information).

## ■ RESULTS AND DISCUSSION

The OM-image of the residue obtained from a droplet with ~120 pg/$\mu$L TMV concentration reveals a structured interface with extensions normal to the rim toward neighboring pillars (Figure 1A Figure S1A, B in the Supporting Information). Other types of morphologies, detached from the main residue, are observed at a larger distance from the rim, corresponding to earlier times of evaporation. Indeed, the SEM image of a central patch on a pillar reveals overlapping lamellae which are slightly rotated against each other (Figure 1A; inset) An extension resembling part of the structured rim reveals the formation of root-like extensions on the pillar suggesting extensional flow-alignment (Figure 1B). A patch of stacked rows of laterally assembled nanoparticles is observed on one of the "roots" (Figure 1B; inset). The strongly binned (32 × 32) RD-image of the interface extension reveals density modulations resembling the morphology of the OM-image (Figure 1C). A zoom shows
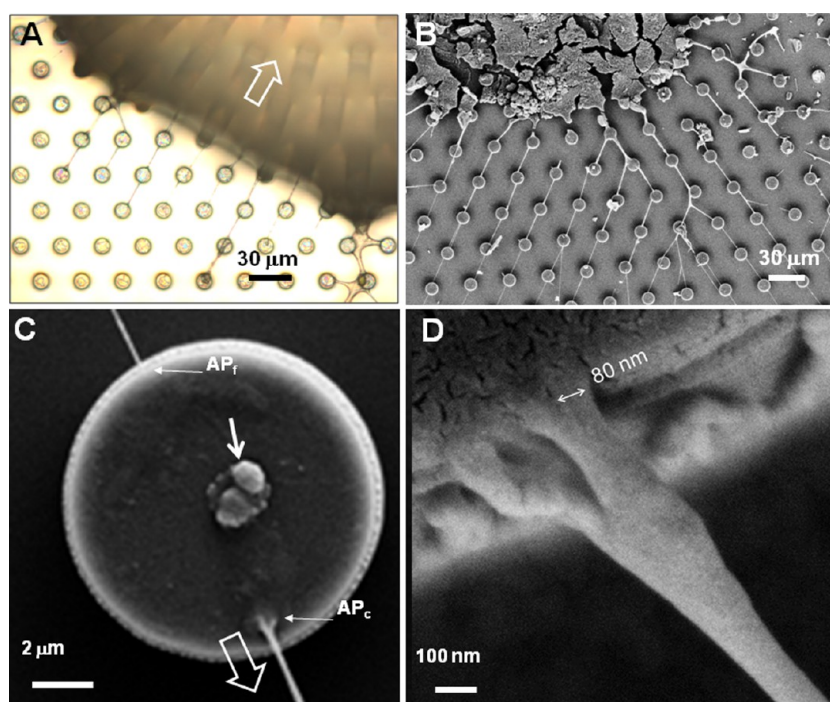
**Figure 2.** (A) OM-image of TMV nanofilaments being pulled out from the droplet interface at an advanced stage of evaporation. The interface retraction direction is indicated by an arrow. (B) SEM image of residue. Nanofilaments are radiating from a central mass of buffer salt residue. (C) SEM image of Si-pillar with nanofilaments attached at positions further away ($AP_f$) and closer ($AP_c$) to the center of the residue. The directions of pulling and interface retraction are indicated by an open arrow. A patch of TMV residue on the pillar is indicated by an arrow. (D) SEM image of $AP_c$ revealing several subfilaments merging into a nanofilament.
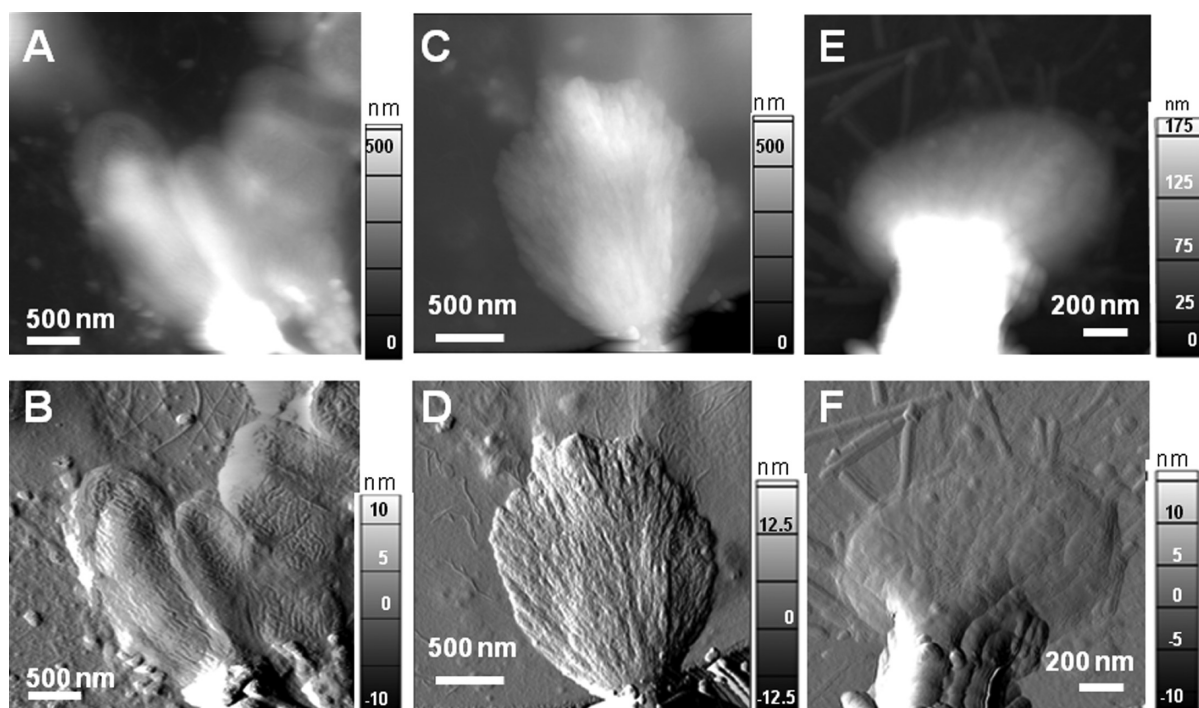


**Figure 3.** (A) AFM topography profile map of $AP_c$ with several patches which are attached to subfilaments. (B) AFM amplitude error image corresponding to A; (C) AFM topography profile image of patch revealing the alignment toward a nanofilament in more detail; (D) AFM amplitude error image corresponding to C; (E) AFM topography profile map of smaller patch attached to nanofilament surrounded by individual TMV nanoparticles. (F) AFM amplitude error image corresponding to E. The scale bars indicate the height. The mean set point amplitude for the acquisition of the images is 135 nm for B, 75 nm for D, and 65 nm for F.

a domain of a few $\mu$m size defined by the 100/110 reflections of the hexagonal TMV lattice (Figure 1D).[11] The alignment and symmetry of the reflections suggests an equatorial fiber texture (Figures 1D, E). The absence of $n = 3/-3$ layer-lines[11] could
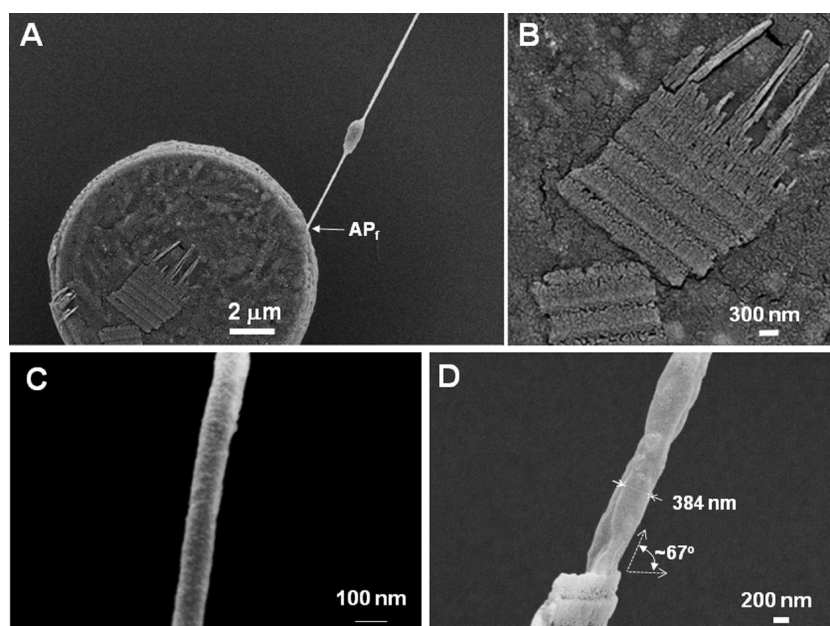
**Figure 4.** (A) SEM image of sheets composed of stacked rows of laterally assembled nanoparticles on top of a pillar. Note the nanofilament at the $AP_f$. (B) Zoom of sheet splitting up into a filamentous morphology at its end. (C) SEM image of a ∼100 nm diameter nanofilament. (D) SEM image of larger nanofilament revealing a transition of stacked rows of nanoparticles into twisted platelets. The angle between the stacked rows and the nanofilament axis is ∼67°.

be due to lack in lateral correlations resulting in diffuse layer-lines or a tilting of the fiber-axis (*c*-axis) out of the pillar surface, which is also observed for the tilting of the extension in Figure 1B. A hexatic columnar mesophase is less probable on grounds of the narrow Gaussian profile shapes. To verify the presence of layer-lines, diffraction experiments in tilting geometry will be required. We also observe the $n = 3/-3$ layer-lines at the rim between the pillars (not shown) and at the residue rim on a wetting substrate.[11] At the onset of the extension, near the center of the pillar, the patterns reveal several lamellar domains that are rotated against each other as expected from the morphology of the central patch shown in Figure 1A (inset).

By reducing the TMV concentration to ∼1.2 pg/μL one can generate nanofilaments extending across a range of pillars (Figures 2A, B). The diameter of the nanofilaments increases from a minimum value of ∼80 nm with decreasing distance from the rim. The more soluble K-phosphate buffer precipitates at the last stage of evaporation (Figure 2B). Nanofilaments are generally bridging the 20 μm gap between neighboring pillars (Figures 2B, C) with anchoring points ($AP_c$; $AP_f$) at opposite edges of a pillar (Figure 2C). The $AP_c$ serves for "pulling" the nanofilament from the retreating droplet interface. The smallest diameter nanofilaments appear to be composed of a single filament but SEM reveals also composite morphologies of several smaller filaments (called here subfilaments) at the $AP_c$. (Figure 2D) The subfilament diameter, corresponding also to the smallest observed nanofilament diameter, is ∼80 nm implying an aspect ratio of ∼250 for a ∼20 μm long nanofilament. As for the higher TMV concentration, we observe other types of residues on the pillars which can best be visualized by AFM in Figures 3A−F. We are showing both the topography profile maps and the amplitude error image. The latter image allows enhancing small morphological details.[37] Indeed, the $AP_c$'s of several subfilaments are surrounded by broad patches (Figure 3A). The AFM amplitude error image reveals fine striations close to the subfilaments due

to flow-alignment, whereas a more random orientation is observed at the opposite side of the patches (Figure 3B). The image suggests also the superposition of layers. The flow-alignment of the TMV nanoparticles in a patch can be better seen in Figure 3C and its amplitude error image (Figure 3D). The AFM topography profile map of a smaller patch suggests also layering which (Figure 3E) is more clearly revealed in the amplitude error image (Figure 3F). We also observe sheets of stacks of laterally assembled nanoparticles (Figures 4A, B) which are attributed to remnants of the wetting layer moving across the pillar during evaporation (see below and Figure S2 in the Supporting Information). This morphology is also observed at the higher TMV concentration (Figure 1B; inset). In view of the concentration-dependent phase transitions of TMV in the presence of salt[14] we assume that a nanofilament, anchored to an $AP_c$, is pulled from a liquid-crystalline interface layer. This pulling can be observed in situ via a sequence of OM-images (see Figure S2 in the Supporting Information). Indeed, the interface layer moves within ∼12 s across the top of the chosen pillar prior to the pulling of a nanofilament. The top of the pillar remains wetted during this movement. As the droplet interface arrives at the pillar-edge it dewets and "jumps" to a neighboring pillar within a shorter time than a single frame (0.58 s), whereas a nanofilament is pulled. Details of the wetting/dewetting process on the pillar are currently unexplored but other results suggest that, prior to its jump, the interface will somewhat move beyond the pillar edge, thus increasing its contact angle for geometric reasons and weakening its wetting properties.[38] The attachment of the nanofilament just below the top of the neighboring pillar at the $AP_f$ suggests that the initial contact after the jump is made at the edge of the pillar implying again a higher contact angle. The interface then moves to the surface of the pillar and the contact angle is reduced in the wetting regime. The time scale of surface tension driven shape changes during water droplet coalescence is in the sub-100 ms range.[39]
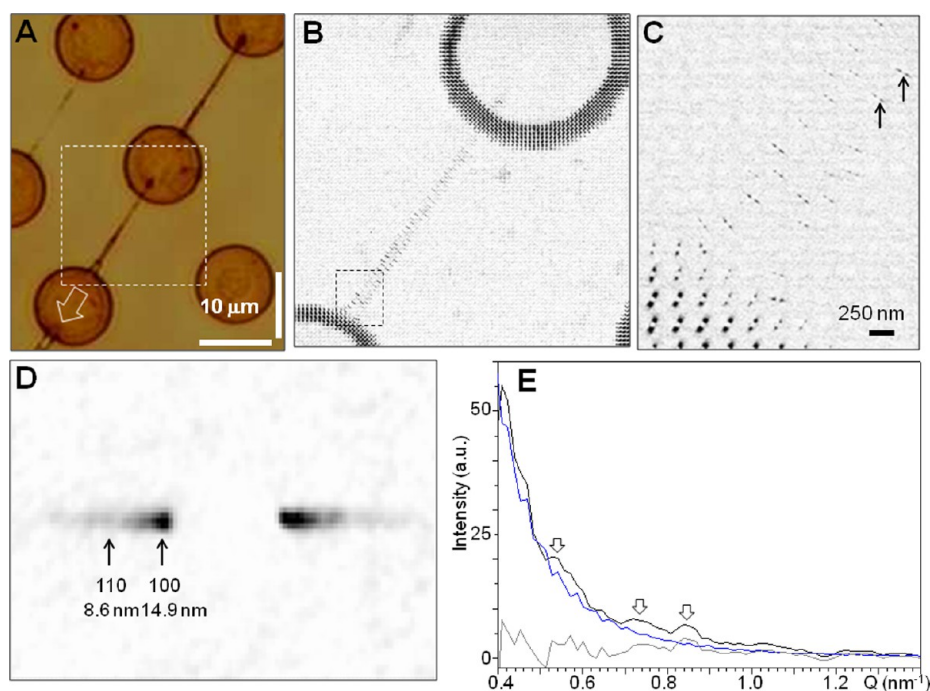
**Figure 5.** (A) OM-image of nanofilaments attached to pillars with a gradient pattern. The direction of interface retraction is indicated by an arrow. (B) RD-image of the dashed area in (A) for a step-size of 0.25 $\mu$m. The Q-range of the pixels is limited to $Q_{max} \approx 0.8$ nm$^{-1}$ ($d \approx 7.8$ nm). The edge of the SU-8 pillars shows strong interface scattering. (C) Splitting of nanofilament into two subfilaments for the dashed area in B. Two of the four streaks used for averaging are indicated by arrows. (D) Scattering from the averaged subfilament streaks, which are located within 1.4 $\mu$m along the right subfilament in 5C. The positions of the hexagonal TMV 100/110 reflections[11] are indicated (see also Figures 1E, F). (E) Radial intensity profile from the azimuthally averaged streak. The low-Q limit is at the beamstop cutoff. The blue profile corresponds to simulated cylindrical scattering with a Gaussian distribution of 75 nm mean radius and $\sigma = 5$ nm. The gray curve corresponds to the difference of experimental and simulated data. The open arrows design peaks not matched by the simulation.

SEM images of selected nanofilaments are shown in Figures 4C, D. The ~100 nm diameter nanofilament (Figure 4C) shows a round cross-section, whereas the thicker nanofilament (Figure 4D) reveals in its lower part stacks of nanoparticles that are tilted against the nanofilament axis. In the upper part, the morphology is transformed into a string of elongated platelets that are twisting along the nanofilament axis (Figure 4D).The nanoparticle assembly in the lower part resembles curled-up sheets shown in Figures 4A, B, suggesting that a ribbon of self-assembled nanoparticles is pulled from the structured droplet interface and wound into a nanofilament. The SEM data do not, however, allow for distinguishing between a single sheet forming a hollow tube or several layers of sheets, as shown schematically in Figure S3A, B in the Supporting Information for a nanofilament with a diameter at the lower limit of the observed values.

The OM-image of several nanofilaments attached to pillars and a RD-image of a single nanofilament are shown in Figures 5A, B. The RD-image of the nanofilament is defined by streaks which are oriented normal to its axis. A close-up allows for observing a splitting into two subfilaments (Figure 5C) that can already be distinguished in the RD-image at the AP$_c$ (see Figure S4A, B in the Supporting Information). The position of the individual subfilaments in Figure 5B is generally revealed by a single streak and sometimes by an additional weaker, neighboring streak. This implies that the size of a subfilament is in the range of the ~170 nm beam size. We have averaged the streaks from four closely neighboring probing-points on the right subfilament in Figure 5C to increase the counting statistics (Figure 5D) The streak does not reveal well-defined spots due

to hexagonal TMV reflections as for the fibrous extension (Figures 1E, F).[11] Its radial intensity profile (Figure 5E) could be due to form-factor scattering from nanoparticles[16] or from the subfilament itself, which is only larger in diameter by about a factor of 10. We have simulated the intensity profile according to[34,40]

$$I(Q) = c \int_o^\infty \frac{r^4}{Q} \left( \frac{2J_1(Qr)_1}{Qr} \right)^2 P(r, \overline{r}, \sigma)dr \tag{1}$$

Where $J_1$ corresponds to a Bessel function of first kind and first order, $c$ is a scaling constant, and $r$ the cylinder radius. The Gaussian term $P(r,\overline{r},\sigma)$ with average cylinder radius $\overline{r}$ and standard deviation $\sigma$ allows introducing a variability of radii.[34] For scattering from TMV nanoparticles with cylindrical geometry and discrete radii of 7.5 nm, the Gaussian term can be neglected and eq S1 in the Supporting Information used. The simulated intensity profile has its first Bessel function minimum at Q ~ 0.46 nm$^{-1}$ (see Figure S5 in the Supporting Information) which is not observed in the experimental intensity profile (Figure 5E). Form-factor scattering from the subfilament was simulated by assuming a cylinder with 75 nm radius. This allows generating orders matching in position the observed intensity modulations but not their small amplitudes (see Figure S5 in the Supporting Information). The intensity profile can, however, be quite well simulated by applying the Gaussian term in eq 1 with $\overline{r} = 75nm$ and $\sigma = 5nm$ (Figure 5E).[34] The $\overline{r}$-value is in the range of the observed nanofilament radii. This result favors the more space-filling morphology of several layers shown schematically in Figure S3B in the Supporting Information. The Gaussian distribution of radii

implies a fluctuation of the cylindrical diameter, possibly because of morphological substructures such as the platelets that are observed for somewhat thicker nanofilaments (Figure 4D). We note several weak and broad peaks (arrows in Figure 5E) that are not matched by the simulations and also cannot be indexed for the hexagonal TMV structure.[11] A possible structure could consist of layers of nanoparticles based on the observed sheets (Figure 4B). Indeed, we tentatively index the $Q$ = 0.56 nm$^{-1}$ peak ($d$ = 11.2 nm) as 11 reflection of a square lattice. This would imply 15.8 nm unit cell vectors normal and parallel to the nanorod direction corresponding to the separation of two neighboring nanorods and 7× the pitch along the nanorod (7 × 2.26 nm). The peaks are, however, too few and too broad to allow determining a lattice at the present stage. It will therefore be interesting probing smaller diameter nanofilaments with possibly fewer and better ordered nano-particles shells (Figure S3A, B in the Supporting Information). Transmission electron microscopy might also shed more light on the morphology of the thinnest nanofilaments.

## CONCLUSIONS

TMV nanoparticles form residues with filamentous extensions on a pillared superhydrophobic substrate. X-ray nanodiffraction probing of an extension reveals crystalline domains with an alignment of the cylindrical nanoparticles along the flow-direction. Nanofilaments can be obtained by reducing the nanoparticle concentration. NanoXRD probing of individual nanofilaments shows some evidence for crystallinity but is dominated by form-factor scattering

The pillar-assisted pulling of nanofilaments from a retracting, structured droplet interface resembles microscale gel spin-ning.[41] Combining nanofilament formation on a smart surface with nanoXRD probing could be applied to other proteins available only in ultrasmall quantities, either by being precious or not yet production-optimized. Examples are $\beta$-sheet materials such as silk protein fibers spun in nature,[42] designer silk proteins,[43−46] or amyloidal nanofilaments,[47] which are currently being probed principally by AFM and SEM techniques.

## ASSOCIATED CONTENT

### Ⓢ Supporting Information

The following experimental details: (i) SR scattering techniques and detector calibration, (ii) AFM imaging, (iii) coffee-ring formation and interface dynamics, (iv) nanofilament models and simulation of equatorial scattering. This material is available free of charge via the Internet at http://pubs.acs.org.

## AUTHOR INFORMATION

### Corresponding Author
*Tel.: +33476882051. E-mail: riekel@esrf.fr.

### Author Contributions
The manuscript was written through contributions of all authors. All authors have given approval to the final version of the manuscript.

### Notes
The authors declare no competing financial interest.

## ACKNOWLEDGMENTS

## REFERENCES

(1) Ryan, A. J.; Terrill, N. J.; Fairclough, J. P. A., A Scattering Study of Nucleation Phenomena in Homopolymer Melts. In *Scattering from Polymers. Characterization by X-rays, Neutrons, and Light*; Cebe, P., Hsiao, B. S., Lohse, D. J., Eds.; ACS Symposium Series: Boston, 1999; Vol. *739*.

(2) Zafeiropoulos, N.; Davies, R. J.; Roth, S. V.; Burghammer, M.; Schneider, K.; Riekel, C.; Stamm, M. Microfocus X-Ray Scattering Scanning Microscopy for Polymer Applications. *Macromol. Rapid Commun.* **2005**, *26*, 1547−1551.

(3) Martel, A.; Burghammer, M.; Davies, R.; DiCola, E.; Panine, P.; Salmon, J. B.; Riekel, C. A Microfluidic Cell for Studying the Formation of Regenerated Silk by Synchrotron Radiation Small- and Wide-Angle X-Ray Scattering. *Biomicrofluidics* **2008**, *2*, 024104.

(4) Martel, A.; Burghammer, M.; Davies, R. J.; Cola, E. D.; Vendrely, C.; Riekel, C. Silk Fiber Assembly Studied by Synchrotron Radiation SAXS/WAXS and Raman Spectroscopy. *J. Am. Chem. Soc.* **2008**, *130*, 17070−17074.

(5) Berthier, J. *Microdrops and Digital Microfluidics*; William Andrew: Norwich, NY, 2008.

(6) Accardo, A.; Fabrizio, E. D.; Limongi, T.; Marinaro, G.; Riekel, C. Probing Droplets on Superhydrophobic Surfaces by Synchrotron Radiation Scattering Techniques. *J. Synchrotron Radiat.* **2014**, *21*, 643−653.

(7) Deegan, R. D.; Bakajin, O.; Dupont, T. F.; Huber, G.; Nagel, S. R.; Witten, T. A. Capillary Flow as the Cause of Ring Stains from Dried Liquid Drops. *Nature* **1997**, *389*, 827−829.

(8) Gentile, F.; Moretti, M.; Limongi, T.; Falqui, A.; Bertoni, G.; Scarpellini, A.; Santoriello, S.; Maragliano, L.; Zaccaria, R. P.; Di Fabrizio, E. Direct Imaging of DNA Fibers: The Visage of Double Helix. *Nano Lett.* **2012**, *12*, 6453−6458.

(9) Henegariu, O.; Grober, L.; Haskins, W.; Bowers, P. N.; State, M. W.; Ohmido, N.; Bray-Ward, P.; Ward, D. C. Rapid DNA Fiber Technique for Size Measurements of Linear and Circular DNA Probes. *Biotechniques* **2001**, *31*, 246−250.

(10) Kendall, A.; McDonald, M.; Bian, W.; Bowles, T.; Baumgarten, S. C.; Shi, J.; Stewart, P. L.; Bullitt, E.; Gore, D.; Irving, T.; Havens, W. M.; Ghabrial, S. A.; Wall, J. S.; Stubbs, G. Structure of Flexible Filamentous Plant Viruses. *J. Virol.* **2008**, *82*, 9546−9554.

(11) Gebhardt, R.; Teulon, J. M.; Pellequer, J. L.; Burghammer, M.; Colletier, J. P.; Riekel, C. Virus Particle Assembly into Crystalline Domains Enabled by the Coffee Ring Effect. *Soft Matter* **2014**, *10*, 5458−5462.

(12) Caspar, D. L. D. Assembly and Stability of the Tobacco Mosaic Virus Particle. *Adv. Protein Chem.* **1963**, *18*, 37−121.

(13) Klug, A. The Tobacco Mosaic Virus Particle: Structure and Assembly. *Philos. Trans. R. Soc., B* **1999**, *354*, 531−535.

(14) Dogic, Z.; Fraden, S. Ordered Phases of Filamentous Viruses. *Curr. Opin. Colloid Interface Sci.* **2006**, *11*, 47−55.

(15) Lu, B.; Stubbs, G.; Culver, J. N. Carboxylate Interactions Involved in the Disassembly of Tobacco Mosaic Tobamovirus. *Virology* **1996**, *225*, 11−20.

(16) Yang, L.; Wang, S. T.; Fukuto, M.; Checco, A.; Niu, Z. W.; Wang, Q. Structure and Interaction in 2D Assemblies of Tobacco Mosaic Viruses. *Soft Matter* **2009**, *5*, 4951−4961.

(17) Britt, D. W.; Buijs, J.; Hlady, V. Tobacco Mosaic Virus Adsorption on Self-Assembled and Langmuir-Blodgett Monolayers Studied by TIRF and SFM. *Thin Solid Films* **1998**, *327*, 824−828.

(18) Wargacki, S. P.; Pate, B.; Vaia, R. A. Fabrication of 2D Ordered Films of Tobacco Mosaic Virus (TMV): Processing Morphology Correlations for Convective Assembly. *Langmuir* **2008**, *24*, 5439−5444.

(19) Dogic, Z.; Philipse, A. P.; Fraden, S.; Dhont, J. K. G. Concentration-Dependent Sedimentation of Colloidal Rods. *J. Chem. Phys.* **2000**, *113*, 8368−8380.

(20) Rammensee, S.; Slotta, U.; Scheibel, T.; Bausch, A. R. Assembly Mechanism of Recombinant Spider Silk Proteins. *Proc. Natl. Acad. Sci. U. S. A.* **2008**, *105*, 6590−6595.

(21) Heddle, J. G. Protein Cages, Rings and Tubes: Useful Components of Future Nanodevices? *Nanotechnol., Sci. Appl.* **2008**, *1*, 67−78.

(22) Rong, J. H.; Oberbeck, F.; Wang, X. N.; Li, X. D.; Oxsher, J.; Niu, Z. W.; Wang, Q. Tobacco Mosaic Virus Templated Synthesis of One Dimensional Inorganic-Polymer Hybrid Fibres. *J. Mater. Chem.* **2009**, *19*, 2841−2845.

(23) Uchida, M.; Klem, M. T.; Allen, M.; Suci, P.; Flenniken, M.; Gillitzer, E.; Varpness, Z.; Liepold, L. O.; Young, M.; Douglas, T. Biological Containers: Protein Cages as Multifunctional Nanoplatforms. *Adv. Mater.* **2007**, *19*, 1025−1042.

(24) Schlick, T. L.; Ding, Z. B.; Kovacs, E. W.; Francis, M. B. Dual-Surface Modification of the Tobacco Mosaic Virus. *J. Am. Chem. Soc.* **2005**, *127*, 3718−3723.

(25) Kuncicky, D. M.; Naik, R. R.; Velev, O. D. Rapid Deposition and Long-Range Alignment of Nanocoatings and Arrays of Electrically Conductive Wires from Tobacco Mosaic Virus. *Small* **2006**, *2*, 1462−6.

(26) Knez, M.; Sumser, M.; Bittner, A. M.; Wege, C.; Jeske, H.; Martin, T. P.; Kern, K. Spatially Selective Nucleation of Metal Clusters on the Tobacco Mosaic Virus. *Adv. Funct. Mater.* **2004**, *14*, 116−124.

(27) Niu, Z.; Bruckman, M.; Kotakadi, V. S.; He, J.; Emrick, T.; Russell, T. P.; Yang, L.; Wang, Q. Study and Characterization of Tobacco Mosaic Virus Head-to-Tail Assembly Assisted by Aniline Polymerization. *Chem. Commun.* **2006**, 3019−3021.

(28) Niu, Z.; Bruckman, M. A.; Li, S.; Lee, L. A.; Lee, B.; Pingali, S. V.; Thiyagarajan, P.; Wang, Q. Assembly of Tobacco Mosaic Virus into Fibrous and Macroscopic Bundled Arrays Mediated by Surface Aniline Polymerization. *Langmuir* **2007**, *23*, 6719−24.

(29) Niu, Z.; Liu, J.; Lee, L. A.; Bruckman, M. A.; Zhao, D.; Koley, G.; Wang, Q. Biological Templated Synthesis of Water-Soluble Conductive Polymeric Nanowires. *Nano Lett.* **2007**, *7*, 3729−33.

(30) Gerasopoulos, K.; Pomerantseva, E.; McCarthy, M.; Brown, A.; Wang, C.; Culver, J.; Ghodssi, R. Hierarchical Three-Dimensional Microbattery Electrodes Combining Bottom-Up Self-Assembly and Top-Down Micromachining. *ACS Nano* **2012**, *6*, 6422−6432.

(31) Miele, E.; Malerba, M.; Dipalo, M.; Rondanina, E.; Toma, A.; Angelis, F. D. Controlling Wetting and Self-Assembly Dynamics by Tailored Hydrophobic and Oleophobic Surfaces. *Adv. Mater.* **2014**, *26*, 4179−83.

(32) Limongi, T.; Cesca, F.; Gentile, F.; Marotta, R.; Ruffilli, R.; Barberis, A.; Maschio, M. D.; Petrini, E. M.; Santoriello, S.; Benfenati, F.; DiFabrizio, E. Nanostructured Superhydrophobic Substrates Trigger the Development of 3D Neuronal Networks. *Small* **2013**, *9*, 402−412.

(33) Marinaro, G.; Accardo, A.; Angelis, F. D.; Dane, T.; Weinhausen, B.; Burghammer, M.; Riekel, C. A Superhydrophobic Chip based on SU-8 Photoresist Pillars Suspended on a Silicon Nitride Membrane. *Lab Chip* **2014**, *14*, 3705−3709.

(34) Mueller, M.; Czihak, C.; Vogl, G.; Fratzl, P.; Schober, H.; Riekel, C. Direct Observation of Microfibril Arrangement in a Single Native Cellulose Fiber by Microbeam Small-Angle X-Ray Scattering. *Macromolecules* **1998**, *31*, 3953−3957.

(35) Schroer, C. G.; Boye, P.; Feldkamp, J.; Patommel, J.; Schropp, A.; Schwab, A.; Stephan, S.; Burghammer, M.; Schoeder, S.; Riekel, C. Coherent X-Ray Diffraction Imaging with Nanofocused Illumination. *Phys. Rev. Lett.* **2008**, *101*, 090801.

(36) Riekel, C.; Burghammer, M.; Davies, R.; Gebhardt, R.; Popov, D., Fundamentals of Non-Crystalline Diffraction with Microfocus Techniques. In *Applications of Synchrotron Light to Non-Crystalline Diffraction in Materials and Life Sciences*; García-Gutiérrez, M., Nogales, A., Gómez, M., Ezquerra, T. A., Eds.; Springer: Heidelberg, 2008.

(37) Stark, M.; Moeller, C.; Mueller, D. J.; Guckenberger, R. From Images to Interactions: High-Resolution Phase Imaging in Tapping-Mode Atomic Force Microscopy. *Biophys. J.* **2001**, *80*, 3009−3018.

(38) Oliver, J. F.; Huh, C.; Mason, S. G. Resistance to Spreading of Liquids by Sharp Edges. *J. Colloid Interface Sci.* **1977**, *59*, 568−581.

(39) Accardo, A.; Mecarini, F.; Leoncini, M.; Brandi, F.; Di Cola, E.; Burghammer, M.; Riekel, C.; Di Fabrizio, E. Fast, Active Droplet Interaction: Coalescence and Reactive Mixing Controlled by Electro-wetting on a Superhydrophobic Surface. *Lab Chip* **2013**, *13*, 332−335.

(40) Glatter, O.; Kratky, O., Small Angle Scattering. In *Small Angle Scattering*; Glatter, O., Kratky, O., Eds.; Academic Press: New York, 1982.

(41) Ziabicki, A. *Fundamentals of Fiber Formation*; John Wiley and Sons: London, 1976.

(42) Vollrath, F.; Knight, D. P. Liquid Crystalline Spinning of Spider Silk. *Nature* **2001**, *410*, 541−548.

(43) Vendrely, C.; Ackerrschott, C.; Roemer, L.; Scheibel, T. Molecular Design of Performance Proteins with Repetitive Sequences: Recombinant Flagelliform Spider Silk as Basis for Biomaterials. *Methods Mol. Biol.* **2008**, *474*, 3−14.

(44) Stark, M.; Grip, S.; Rising, A.; Hedhammar, M.; Engstroem, W.; Hjaelm, G.; Johansson, J. Macroscopic Fibers Self-Assembled from Recombinant Miniature Spider Silk Proteins. *Biomacromolecules* **2007**, *8*, 1695−1701.

(45) Oroudjev, E.; Soares, J.; Arcidiacono, S.; Thompson, J. B.; Fossey, S. A.; Hansma, H. G. Segmented Nanofibers of Spider Dragline Silk: Atomic Force Microscopy and Single-Molecules Force Spectroscopy. *Proc. Natl. Acad. Sci. U.S.A.* **2002**, *99*, 6460−6465.

(46) Ling, S.; Li, C.; Adamcik, J.; Wang, S.; Shao, Z.; Chen, X.; Mezzenga, R. Directed Growth of Silk Nanofibrils on Graphene and Their Hybrid Nanocomposites. *ACS Macro Lett.* **2014**, *3*, 146−152.

(47) Knowles, T. P. J.; Buehler, M. J. Nanomechanics of Functional and Pathological Amyloid Materials. *Nat. Nanotechnol.* **2011**, *6*, 469−479.